Origin of Vanadium Site Sequential Oxidation in KxVPO4F1–yOy

Romain Wernert, Antonella Iadecola, Lorenzo Stievano, Dany Carlier, Laurence Croguennec

Origin of vanadium site sequential oxidation in $K_xVPO_4F_{1-y}O_y$

Romain Wernert[1,2,3], Antonella Iadecola[3], Lorenzo Stievano[2,3,4], Dany Carlier[1,3,4,*], Laurence Croguennec[1,3,4,*]

AUTHOR ADDRESS

[1] Univ. Bordeaux, CNRS, Bordeaux INP, ICMCB, UMR 5026, F-33600 Pessac, France

[2] ICGM, Univ. Montpellier, CNRS, ENSCM, 34095 Montpellier, France

[3] RS2E, Réseau Français sur le Stockage Electrochimique de l'Energie, FR CNRS #3459, Amiens F-80039 Cedex 1, France

[4] ALISTORE-ERI European Research Institute, FR CNRS 3104, F-80039 Amiens Cedex 1, France

ABSTRACT:

M-ion batteries (M = Li, Na, K…) positive electrode materials most often operate through the reversible oxidation of transition metal ions. In complex materials involving many transition metals or many redox centres, understanding the sequence in which they participate to the reaction is not trivial but is often necessary to explain the electrochemical properties. Mixed anion vanadium phosphates such as $KVPO_4F_{0.5}O_{0.5}$ are known to contain two different redox entities that are $V^{3+}O_4F_2$ and $V^{3+}O_5F$ "ionic" entities on one hand and $\{V^{4+}{=}O\}O_5$ and $\{V^{4+}{=}O\}O_4F$ "covalent" vanadyl type units on the other hand. However, their participation to the redox mechanism occurring during the charge of this material has never been studied. Here we use V K-edge X-ray absorption spectroscopy to unveil the redox mechanism of $KVPO_4F_{1-y}O_y$ (y = 0, 0.5, 1), performing data analysis via a chemometric approach. Being XAS very sensitive to the oxidation state and bond length, it was found that the ionic V^{3+}—F units oxidize at a lower potential than the covalent $\{V^{4+}{=}O\}$ ones, which is surprising considering the high electronegativity of fluoride anions, but consistent with the redox potential observed for $KVPO_4F$ and $KVOPO_4$. Further a*b initio* calculations and *ex situ* X-ray diffraction analyses allowed an atomistic description of the redox mechanism with the sequential oxidation of the *cis* V site before the *trans* V site in $KVPO_4F$ upon charge. Finally, the complete atomically-resolved redox mechanism of $KVPO_4F_{0.5}O_{0.5}$ is proposed.

INTRODUCTION

K-ion batteries (KIBs) were introduced as an alternative technology to Li-ion batteries (LIBs) for which the need in critical metals can be a severe issue.[1–3] KIBs can operate with a graphite negative electrode, contrary to Na-ion batteries, and the electrochemical potential of the K^+/K redox couple is even lower than that of Li and Na (Li: -2.8 V *vs.* normal hydrogen electrode (NHE), Na: -2.5 V *vs.* NHE, K: -2.95 V *vs.* NHE, in carbonate solvents).[4,5] As for LIBs, the overall performance at the cell level is strongly dependant on the energy density of the positive electrode. Prussian blue analogues $K_2MFe(CN)_6$ (M = Fe, Mn) and vanadium polyanionic compounds $KVPO_4X$ (X = F, O) are among the most promising cathode materials due to their high theoretical energy density of about 500 to 600 $Wh{\cdot}kg^{-1}$.[1,6,7]

$KVPO_4F$ and $KVOPO_4$ have been already reported as high voltage positive electrode materials for K-ion batteries.[8–10] Both compounds crystallize in the $KTiOPO_4$-type structure where the three dimensional framework consists in infinite corrugated chains of vanadium octahedra held by PO_4 tetrahedra (**Figure 1**). In $KV^{3+}PO_4F$, vanadium ions are coordinated in either *trans* or *cis* VO_4F_2 quasi-symmetric octahedra, F being the corner sharing atom along the chains. In $KV^{4+}OPO_4$, the VO_6 octahedra are distorted and non-centrosymmetric, resulting in short 1.65 Å V=O bonds and a noticeable decrease of V-V distances.[11] Considering the electronic structure, $V^{4+/3+}O_4F_2$ in K_xVPO_4F and $\{V^{5+/4+}{=}O\}O_5$ in K_xVOPO_4 can be seen as two different redox entities with their electrochemical potential governed by their respective metal-ligand ionocovalency.[12] Moreover, to the best of our knowledge, the effect of the anion configuration (*cis* or *trans*) in vanadium phosphate fluoride has never been reported. The structural mechanism upon K^+ de-insertion has already been investigated but there is currently a lack of understanding concerning the charge compensation mechanisms in $KVPO_4F$ and $KVOPO_4$.[9,10]

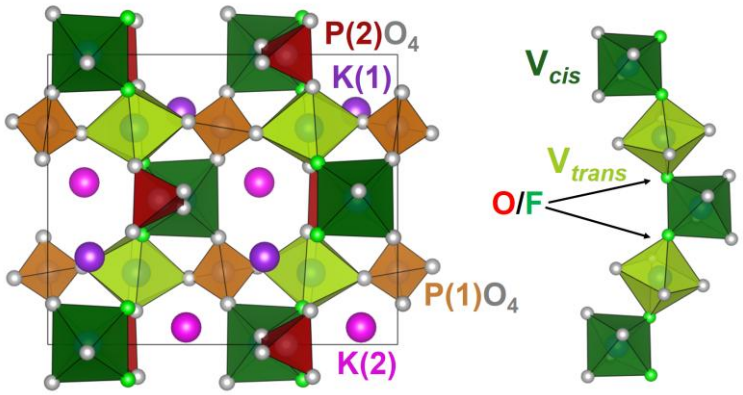

Figure 1: Crystal structure of $KVPO_4F$. The anionic sites bridging vanadium octahedra are selectively occupied by F^- in $KVPO_4F$ or randomly occupied by O^{2-} and F^- in $KVPO_4F_{0.5}O_{0.5}$ thus forming infinite chains of alternating *cis* and *trans* vanadium sites.

In the case of Li- or Na-based vanadium (oxide, fluoride) phosphate such as $LiVPO_4F_{1-y}O_y$ and $Na_3V_2(PO_4)_2F_{3-2y}O_{2y}$ ($0 \leq y \leq 1$), X-ray absorption spectroscopy (XAS) studies revealed that in mixed anion compounds, the $\{V^{4+}{=}O\}O_5$ vanadyl units oxidize before $V^{3+}O_4F_2$ environments upon charging.[13,14] The redox mechanism is surprising given that, in terms of formal oxidation state (*i.e. d* electron count), it implies the activation of $V^{5+/4+}$ before $V^{4+/3+}$, and it was even depicted as a "redox paradox" by Boivin *et al.* in an earlier work of our group.[13] However, a good comprehension of the phenomenon was achieved by referring to the so-called "reversed inductive effect", where the high covalency of {V=O} bond increases the anti-bonding character of the V 3*d* states in $\{V^{4+}{=}O\}O_5$ environments compared to that observed for the V 3*d* states in ionic VO_4F_2 environments in fluorine-

rich compounds, explaining thus the activation of the preferential oxidation of the first V versus the second during charge.[14] In addition, vanadium is prone to unusual redox behaviours such as the dismutation of V^{4+} to V^{5+} and V^{3+} in $Na_1V_2(PO_4)_2F_3$,[14,15] as well as noticeable changes in the coordination geometry such as the transformation of symmetrical $V^{4+}O_6$ octahedra in distorted $\{V^{5+}=O\}O_5$ vanadyl unit upon charge in $Na_4FeV(PO_4)_3$.[16]

Interestingly, recent investigations of $KVPO_4F$ and $KVOPO_4$ indicated that the redox potential of $KVOPO_4$, containing vanadyl bonds, was higher than that of $KVPO_4F$.[11] Intermediate compositions $KVPO_4F_{1-y}O_y$ ($0 \leq y \leq 1$) are reported but the redox mechanism, to the best of our knowledge, has never been investigated.[11] Until now, it is unclear whether the mixed-anion $KVPO_4F_{1-y}O_y$ will behave in the same way as Li- and Na-based vanadium phosphates (i.e., $\{V^{4+}=O\}O_5$ oxidizes before $V^{3+}O_4F_2$) or in the reverse way as it could be expected looking at the redox potential of the end-member compounds. Here, the redox mechanisms of $KVPO_4F$, $KVOPO_4$ as well as $KVPO_4F_{0.5}O_{0.5}$ were probed by *operando* V K-edge XAS during a full charge/discharge cycle. Using a chemometric approach, we show how many independent successive mechanisms occur during K^+ deinsertion and their corresponding V local environments. Further investigations based on DFT calculations and X-ray diffraction for partially de-intercalated $K_{0.5}VPO_4F$ provide complementary insightful information, allowing a full resolution of the redox activity of the two crystallographic V sites (*cis* and *trans*).

METHODS AND EXPERIMENTS

Sample preparation

$KVPO_4F$, $KVOPO_4$ and $KVPO_4F_{0.5}O_{0.5}$ were prepared by solid state high temperature synthesis in argon atmosphere as previously reported.[11] After the synthesis, the obtained materials are perfectly stable and can be handled in air. The diffraction patterns of these three compounds are displayed in **Figure S1** and their morphology revealed by scanning electron microscopy in **Figure S2**.

The *operando* experiments were performed using the *in situ* electrochemical cell designed by Leriche *et al*.[17] The front Be window, where the positive electrode sits, was protected with 6.5 µm thin Al foil (Advent research materials Ltd, 99.5 %). The self-standing electrodes were made of 35 wt.% active material, 60 wt.% carbon black (Super P) and 5 wt.% PTFE (Sigma-Aldrich) shaped as 13 mm diameter disks and pressed under 5 tons. The electrode formulation was optimized for allowing XAS measurements at the V K-edge. The high amount of carbon tends to lower the coulombic efficiency of the first cycle but the electrochemical activity of $KVPO_4F$ is maintained (**Figure S3).** The batteries were cycled at 6.55 $mA \cdot g^{-1}$ which corresponds to a C-rate of C/20. A 3 mm diameter hole was drilled in the centre of K metal negative electrode to enable the experiment in transmission mode.

Samples for *ex situ* X-ray diffraction consisted in an active material : carbon black mixture of 70:30 wt.% cycled in a coin cell vs K metal at C/20. The powder was recovered and washed with dimethyl carbonate (Sigma Aldrich, 99%) to remove residual KPF_6 salt.

For all electrochemical experiments, the electrolyte was a 0.8 M solution of KPF_6 (Sigma-Aldrich, ⩾99%) in a 1:1 volumetric mixture of ethylene carbonate (Sigma-Aldrich, anhydrous, 99%) and diethylene carbonate (Sigma-Aldrich, anhydrous, 99%). Viledon fiber mat (Freudenberg) was used as separator between the positive electrode and negative K metal (Alfa Aesar, 99.95%) and the electrochemical cells were assembled in a glovebox under argon atmosphere.

X-ray absorption spectroscopy (XAS)

V K-edge XAS was performed in transmission geometry at the ROCK beamline, Synchrotron SOLEIL (Saint-Aubin, France). A vanadium metal foil was used as the reference for energy calibration of each individual spectrum. The Si (111) Quick-XAS monochromator was set to an

oscillating frequency of 2 Hz and each final spectrum consisted of a ten minutes average acquisition of ≈1 200 individual Quick-XAS spectra. Three electrochemical cells containing the three studied materials were mounted on a linear translation stage and cycled simultaneously. Each cell was exposed to the incident X-ray beam for data collection for 10 minutes every 30 minutes. Energy calibration and normalization were performed with an automatized Python routine developed at the ROCK beamline.[18] The Multivariate Curve Resolution – Alternated Least Square (MCR-ALS) algorithm was applied to analyse each whole XAS datasets collected for the three samples using the MATLAB toolbox developed by Jaumot et al.[19,20] The advantages and the methodology of this analytical approach were previously described in detail by Fehse *et al*.[21] The number of pure components used in the MCR-ALS analysis was determined for each material by Principal Component Analysis of the respective XAS dataset. The MCR-ALS pure components were constrained to be non-negative and the system was considered as closed, meaning that the sum of the pure components was constrained to be equal to 100 % at all time. The fitting of the Extended X-ray absorption fine structure (EXAFS) signal resulting from the MCR-ALS pure components was performed using the DEMETER package. The EXAFS oscillations were fitted in **R**-space with *k*, k^2 and k^3 weights and a sine window (d*k*=0) from 3.8 $Å^{-1}$ to 11.4 $Å^{-1}$ was applied. Only the first coordination shell of V was considered for the fitting and all figures are displayed with k^2 weight. The second shell contains contributions from V-V, V-P and V-K single scattering paths plus multiple scattering paths that could not be successfully disentangled. The transformation from real space back to **q**-space was done with a sine window again (dR=0) from 1 to 2.2 Å. The EXAFS parameter S_0^2 was set to 1 (value refined from the V foil) and E_0 was initially set at absorbance 0.8 before being refined.

Structural analysis

Laboratory powder X-ray diffraction (XRD) was performed on a XPert' 3 instrument operating with a Cu $K_{\alpha1,2}$ source ($\lambda_{K\alpha1}$ = 1.5405 Å, $\lambda_{K\alpha2}$ = 1.5443 Å). The powder samples were packed in 0.3 mm borosilicate glass capillaries. The patterns were recorded between 5 and 90° 2θ with a step size of 0.008° and acquisition time of at least 14 hours. Rietveld refinements were performed using the JANA2006 computer program.[22] A semi-rigid body restraint was applied to the very covalent phosphate groups, allowing the P−O distances to vary between 1.535±0.035 Å.[23] The Bérar-Lelann correction was applied to standard uncertainties.[24] VESTA software was used to visualize the crystal structures and spin density maps and to calculate the Madelung site potentials.[26]

Density functional theory calculations.

First-principles calculations were performed within the density functional theory (DFT) framework, and the calculations using the projector-augmented wave (PAW) method[27,28] were computed with the Vienna *Ab initio* Simulation Package (VASP) code[27,29–32]. The structural relaxation and total energy calculation were performed using the generalized gradient approximation (GGA) with the Perdew-Burke-Ernzerhof (PBE) exchange-correlation functional[33]. The self-interaction error of strongly correlated 3*d* electrons was corrected using the rotationally invariant Dudarev method.[34] The Hubbard correction term for vanadium 3*d* electrons of the $KVPO_4F$ system, U_{eff} (U - J) was set to 4 eV according to previous work.[11] All calculations were spin-polarized with ferromagnetic ordering, and performed with a plane-wave cutoff energy of 600 eV and a *k*-grid of 4 × 4 × 4. The structure refined from synchrotron powder XRD of $KVPO_4F$ reported in an earlier work was used as the input model before structural relaxation.[11] For calculations of the electronic structure of *cis* and *trans* $SrVO_2F$, hypothetical crystal structures were modelled in VESTA and subsequently relaxed with cubic constraint. A single perovskite type unit cell was considered for *trans* $SrVO_2F$ (*k*-grid of 11 × 11 × 11) whereas a 2 × 2 × 2 perovskite supercell was used for *cis* $SrVO_2F$ (*k*-grid of 6 × 6 × 6). The Hubbard correction term for vanadium 3*d* electrons, U_{eff} (U - J) was set to 3 eV. [35]

RESULTS AND DISCUSSION

V K-edge X-ray absorption spectroscopy

$KVOPO_4$ used as a positive electrode material and cycled in the 2.5 – 5 V voltage window (*vs.* K^+/K) can deliver about 70 $mAh \cdot g^{-1}$ reversibly (**Figure S4a**). The capacity arises from the reversible exchange of 0.55 K^+ per unit formula and the charge compensation is expected to be ensured by the oxidation of V^{4+} into V^{5+}. In the pristine compound, vanadium ions are strongly π-hybridized with one oxygen atom ({V=O} bond being 1.65 Å long) resulting in strongly distorted vanadyl-type environments. The removal of centro-symmetry causes a strong metal 3*d*-4*p* mixing, resulting in an intense pre-edge peak at 5469.4 eV (**Figure S4b)**. The same feature is shown in other vanadyl phosphate compounds such as $NaVOPO_4$ (used as a reference here) as well as $LiVOPO_4$ or $Na_3(VO)_2(PO_4)_2F$. The *operando* XANES spectra collected during the first charge of $KVOPO_4$ are presented in **Figure 2a**. The shape of the corresponding electrochemical curve (**Figure S4a**) is in good agreement with the already reported ones despite suffering for a large irreversible capacity.[11] At a first glance, the edge position shifts to higher energy upon K extraction, which implies the oxidation of vanadium. Moreover, the pre-edge region is characterized by a very smooth transformation from an intense initial feature at 5469.4 eV to a second intense feature at higher energy (5470.8 eV). The remaining contribution at ~5469.4 eV in the last spectrum is consistent with the fact less than one e^- per formula unit is exchanged, as the theoretical capacity is not fully achieved. Nevertheless, the pre-edge region is as intense in the pristine and charged states confirming that $\{V^{5+}=O\}O_5$ environments are preserved upon K^+ extraction. The complete reversibility of the redox process is assessed by the perfect superposition of the spectra of pristine and fully discharged samples (**Figure S4b**), despite the observed large irreversible capacity. The latter observation tends to confirm that the low coulombic efficiency of the first cycle is due to electrolyte side reactions and not to V dissolution.[10,11,36–38] Indeed, the irreversible capacity is so large that it would be noticed on the XAS spectra if it was due to V dissolution.[38] Overall, the evolution of the spectra upon charge is fully consistent with the activation of $\{V^{5+/4+}=O\}$ redox couple.

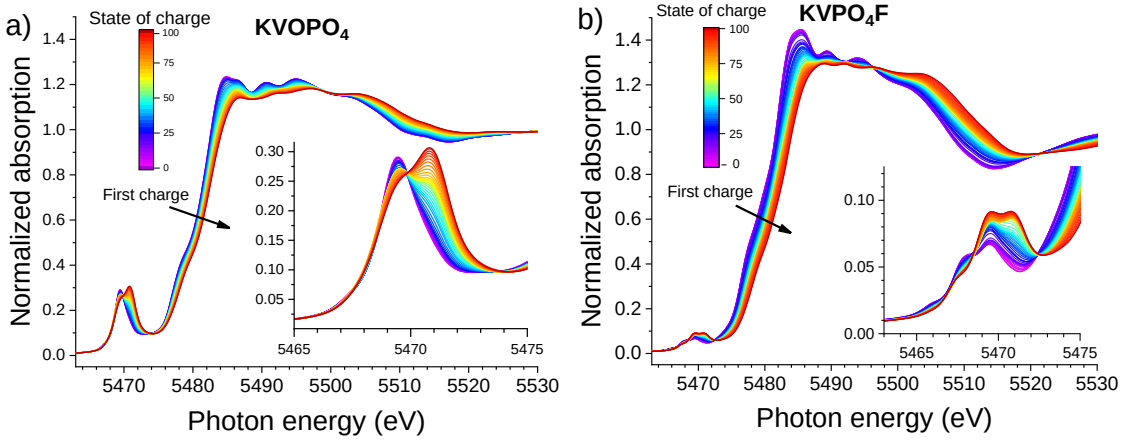

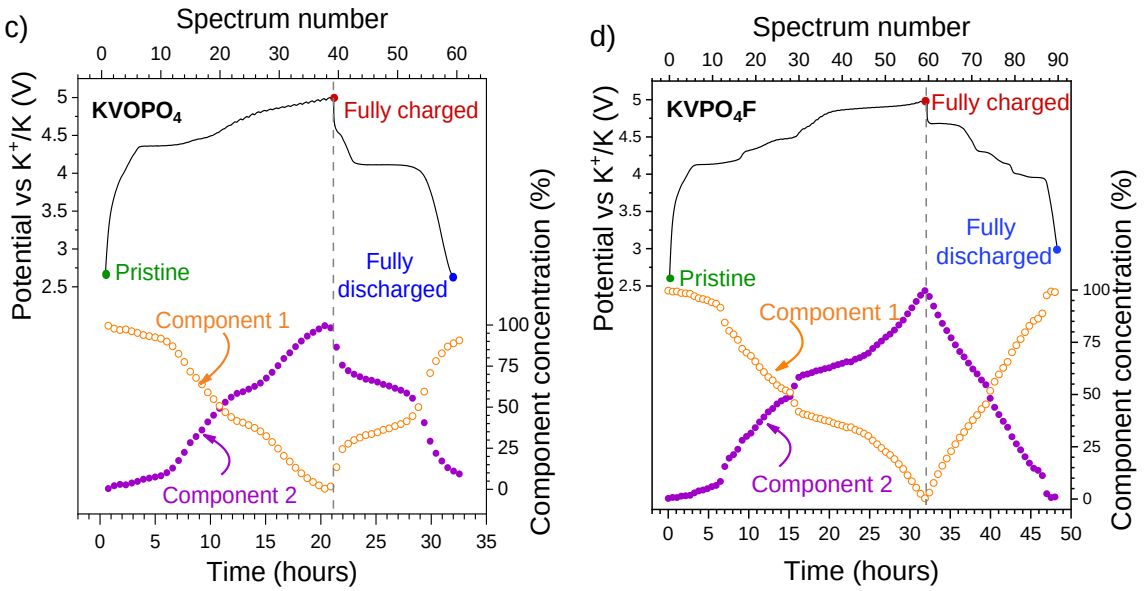

Figure 2: Evolution of the XANES spectra collected *operando* during the first charge of K//$KVOPO_4$ (a) and K//$KVPO_4F$ (b) batteries; a zoom of the pre-edge region is shown in the inset. The corresponding first electrochemical cycles obtained for $KVOPO_4$ (c) and $KVPO_4F$ (d) as well as the concentrations of the respective pure components obtained by the corresponding MCR-ALS analyses.

In the case of $KVPO_4F$, only 0.81 K^+ ions is reversibly exchanged during the first cycle (**Figure S5a**); the corresponding charge transfer mechanism is expected to be the activation of the $V^{4+/3+}$ redox couple. Again, the main edge shifts towards higher energy (**Figure 2b**) during the first charge, and the process is fully reversible (**Figure S5b**). However, a more complex behaviour is observed in the pre-edge region. In the pristine state, two main features can be identified at 5467.8 and 5469.3 eV, separated by 1.5 eV which is the typical value observed in other V^{3+} phosphates.[39,40] In the charged state, the pre-edge region has a similar structure but is shifted towards higher energies by 1.5 eV and is slightly more intense.

MCR-ALS analysis was performed on the whole XAS datasets collected for $KVPO_4F$ and $KVOPO_4$ during the full first charge/discharge cycle. In both cases, only two pure components are needed to express the variance contained in all the individual spectra of the datasets, meaning that the redox mechanism can be described as a single step oxidation in charge and a single step reduction in discharge. In this very simple case, the components were numerically reconstructed and are found to be identical to the pristine and fully charged spectra (**Figures S6** and **S7**). Therefore, all intermediate spectra collected in the two experiments can be obtained by linear combination of the two respective pure components (**Figure S8**). Nevertheless, further insights can be obtained by following the evolution of the relative concentration of each component throughout the first cycle for both compounds (**Figures 2c and 2d**). For $KVOPO_4$, the concentration profiles during charge and discharge are not linear (as it would be expected for the evolution of the redox reaction at the cathode, the current being constant) and are slightly asymmetric despite full reversibility (**Figure S4b**), while for $KVPO_4F$ the concentration profile is very different in charge and discharge. Indeed, in the latter case, the concentration of the two components shows a nearly linear time dependence during the discharge, whereas a plateau region is observed in the concentration profile of $KVPO_4F$, above 4.5 V upon charge, between spectra #30 and #45. This behaviour probably originates from redox side-reactions of the electrolyte at the positive electrode, which hinders the redox reaction at the cathode and the corresponding extraction of K^+ until passivation of the surface of the positive electrode.[38]

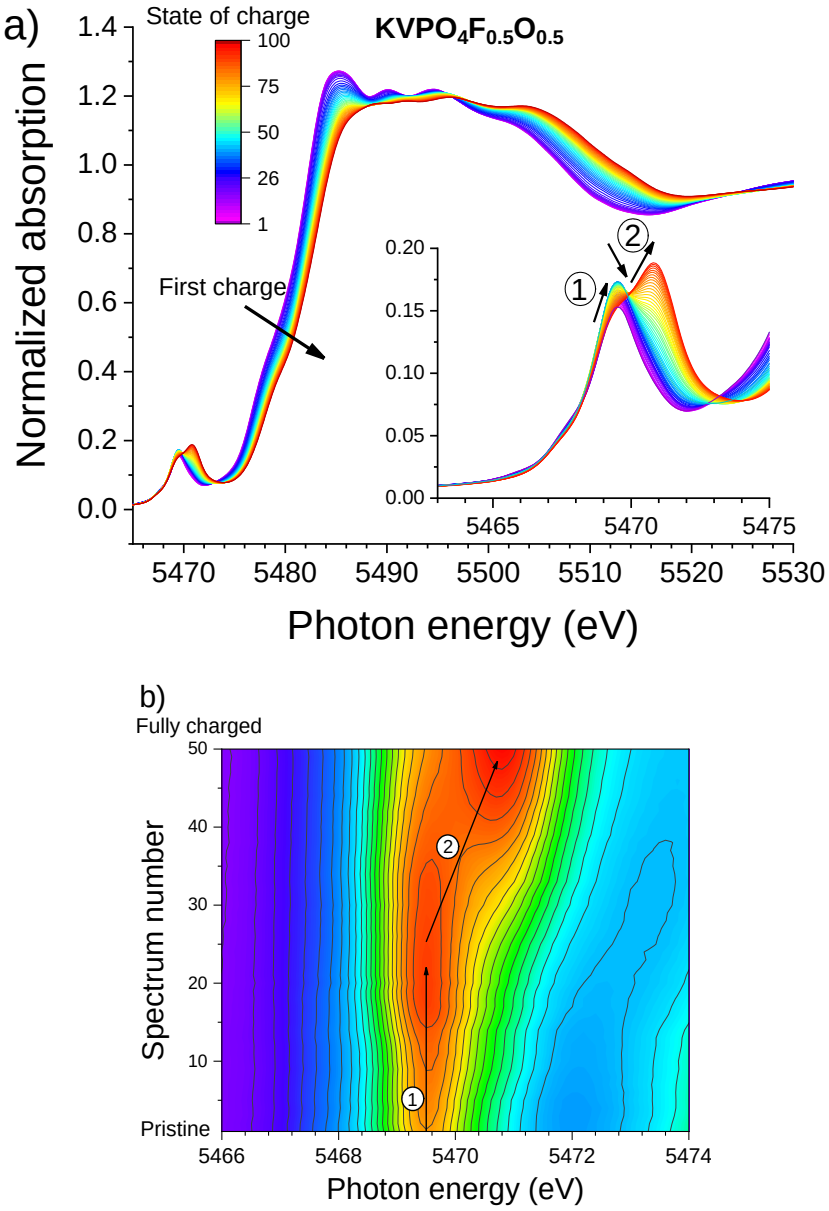

Figure 3: a) Evolution of the XANES spectra collected *operando* during the first charge of K//$KVPO_4F_{0.5}O_{0.5}$ is shown together with a zoom on the pre-edge region, where a two-step evolution is observed. b) Corresponding contour plot of the pre-edge region during the first charge.

Operando XAS was also used to follow the operation of a K//$KVPO_4F_{0.5}O_{0.5}$ battery, and the collected data were subsequently analysed using the same approach previously described for $KVOPO_4$ and $KVPO_4F$. The electrochemical cycling curve (**Figure S9a)** features a small plateau at high K^+ content and then a quasi-smooth slope up to 5 V, showing little inflexion at 4.6 V upon charge. The V K-edge XAS spectra corresponding to the first charge (**Figure 3**) resembles to those already presented for parent compounds. The similarity of the spectra with those of $KVPO_4F$ or $KVOPO_4$ might lead us to think, unwisely, that the redox mechanism is simply the average of the respective mechanisms, but a careful look at the pre-edge reveals more complexity. Indeed, the inset in **Figure 3** shows that, upon charge, the pre-edge evolves in a two-step mechanism. First, the intensity of the feature at 5469.3 eV increases slightly until spectrum #24 and then decreases in favour of the feature observed at 5470.8 eV, reaching a maximum intensity at the end of charge (spectrum #50, **Figure 3b**). Based on the changes observed in the pre-edges upon charge of $KVPO_4F$ and $KVOPO_4$, the first redox activity in $KVPO_4F_{.5}O_{0.5}$ can be attributed to $V^{4+/3+}$ redox couple and the second one to $\{V^{5+/4+}=O\}$. If we related this finding to the different chemical environments of vanadium in the substituted compound, it would

mean that first VO_4F_2 and VO_5F (without vanadyl bonds) environments are oxidized and then the $\{V^{4+}=O\}O_4F$ and $\{V^{4+}=O\}O_5$ environments are triggered at higher potential. This observation is consistent with the redox potential of $KVPO_4F$ and $KVOPO_4$ reported earlier.

In order to confirm the reaction pathways sketched above for $KVPO_4F_{0.5}O_{0.5}$, the *operando* XAS spectra acquired during the first electrochemical cycle was analysed by MCR-ALS. Unlike $KVPO_4F$ and $KVOPO_4$, three independent components are needed in the partially substituted compound in order to form a basis vector set to reconstruct the spectra contained in the XAS dataset (**Figure S10**). The concentration profile of the three components during the experiment as well as the pure components are plotted in **Figure 4**. Components C1 and C3 can be attributed without any doubt to the pristine and end of charge spectra, respectively, as reflected by their concentration reaching 100 % at the beginning of the experiment and at the end of depotassiation, respectively. Component C2 does not correspond to any of the experimental spectra, meaning that it does not appear "pure" in the dataset. Indeed, the concentration of C2 at spectrum #24, just halfway through the complete charge, contains about 10% of the pristine (C1) and 10% of the end of charge (C2) components. This can be explained by the contribution of local inhomogeneities in the electrode, where slightly different states of charge can be encountered in the 2000×800 μm^2 electrode slice probed by the beam.[41] Hence, C2, which reaches maximal concentration at around 4.5 V, corresponds to a chemical formula close to $K_{0.5}V^{4+}PO_4F_{0.5}O_{0.5}$. Interestingly, the slope of the concentration of C3, reverse and complementary to the disappearance of C2, is less steep than that of the transformation of C1 to C2. This indicates that an additional redox process is ongoing during the second oxidation step. Moreover, during the following discharge, C3 vanishes twice as fast as it appears in the charge process. As it was pointed out, side reactions such as electrolyte oxidation are very common issues in K-ion batteries[36–38], especially at high potentials in the first charge cycle; such parasite processes are most probably the cause of such as oxidation reaction.

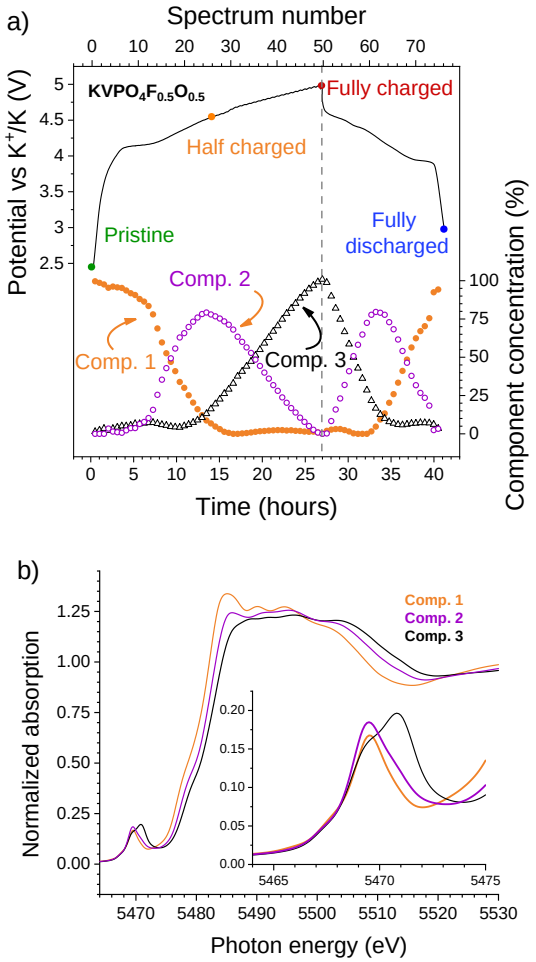

Figure 4: a) First electrochemical cycle obtained for the K//$KVPO_4F_{0.5}O_{0.5}$ cell during the *operando* XAS experiment, and evolution of the concentration of the three pure component resulting from MCR-ALS. b) XANES spectra of the three MCR-ALS pure components.

In addition to first insights on the local geometry and the electronic structure of V sites obtained by the comparison of the XANES spectra, quantitative information on the V-O/F bond-lengths were extracted by the analysis of the EXAFS signals. Only the EXAFS spectra of the reconstructed principal components were fitted, as any intermediated EXAFS spectra can be obtained by their linear combination. The total number of first neighbours was fixed to 6, and two populations of bonds were considered, namely regular V—O/F and short V=O bonds. **Table 1** summarizes the fitting models and results for each component. The first peak of the Fourier transform of $KVPO_4F$ spectra (**Figure S11**) is well described by a symmetric model where the initial average V—O/F bond length is close to 2.01 Å and shrinks to 1.94 Å in the charged state. For $KVOPO_4$ (**Figure S12**), the pristine compound is described by a [5+1] model where the vanadyl bond is initially equal to 1.65 Å, and then shortens to 1.62 Å upon charge. For the partially F-substituted compound $KVPO_4F_{0.5}O_{0.5}$, the first coordination shell is described by an average of the two previous models: a weight of 0.5 is set to consider the short covalent V=O bond and the remaining 5.5 surrounding atoms depicts both regular V—O and V—F bonds.[11] Finally, the fitting of these EXAFS data (**Figure 5**) clearly confirms the sequential activation of both redox couples in $KVPO_4F_{0.5}O_{0.5}$, i.e., a combination of the two previously observed mechanisms. The regular V—O/F bonds slightly shorten during the first step (C1 → C2), followed by the V=O bond shortening in the second step (C2 → C3). In all cases, the Debye-Waller factors are systematically higher for deintercalated compounds compared to the pristine materials, indicating a larger distribution of local environments, consistently with the multiple oxidation state of vanadium in these compounds. Overall, the results of EXAFS analysis also support the interpretation of the

sequential oxidation of first $V^{3+}O/F$ and then $\{V^{4+}=O\}$ containing environments in $KVPO_4F_{0.5}O_{0.5}$. Unfortunately, XAS cannot distinguish between the $V(1)_{cis}$ and $V(2)_{trans}$ crystallographic sites as their local structure is very similar, neither by the XANES nor EXAFS region analyses. For a full atomic description of the redox mechanisms, therefore, the assistance of a complementary approach is necessary. Hence, the electronic structure of K_xVPO_4F (x = 0, 0.5, 1) was further investigated by *ab initio* calculations together with *ex situ* X-ray diffraction.

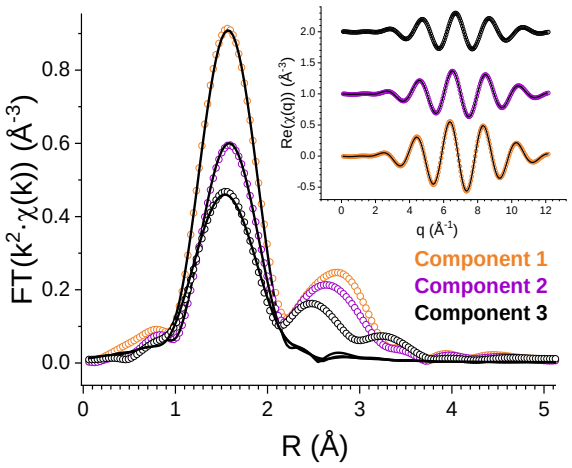

Figure 5: Fits of the first coordination shell of the EXAFS signals of the three MCR-ALS pure components obtained from the *operando* XAS analysis of $K_xVPO_4F_{0.5}O_{0.5}$.

Table 1: Refined EXAFS parameters of each principal component related to the operando XAS datasets for the $K_xVPO_4F_{1-y}O_y$ (y=0, 0.5, 1) compounds.

Compound	Component	Bond	N	R (Å)	Debye-Waller Factor (10^{-2} Å^2)	EXAFS agreement factor (%)
$KVPO_4F$	Component 1	V−O/F	6	2.01(1)	0.51(3)	0.3
	Component 2	V−O/F	6	1.94(1)	0.95(4)	0.3
$KVOPO_4$	Component 1	V−O/F	5	2.01(1)	0.81(5)	0.2
		V=O	1	1.65(1)	0.24(6)	
	Component 2	V−O/F	5	1.95(1)	1.4(1)	0.4
		V=O	1	1.62(1)	0.35(5)	
$KVPO_4F_{0.5}O_{0.5}$	Component 1	V−O/F	5.5	2.02(1)	0.46(5)	0.2
		V=O	0.5	1.65(1)	0.02(2)	
	Component 2	V−O/F	5.5	1.99(3)	1.01(4)	0.2
		V=O	0.5	1.65(1)	0.10(9)	
	Component 3	V−O	5.5	1.96(1)	1.1(1)	0.4
		V=O	0.5	1.60(2)	0.2(2)	

Electronic structure calculations

To achieve better description of the redox mechanism involving the two crystallographic V sites ($V(1)_{cis}$ and $V(2)_{trans}$), we performed GGA+U calculations for the K_xVPO_4F (x = 0, 0.5, 1) system. Only the pure fluorine end-member was considered since a similar study already exists in the literature for $KVOPO_4$.[42] Indeed, Lian *et al.* conducted a full *ab initio* study of K_xVOPO_4 and demonstrated that $V_{cis}O_6$ oxidizes preferentially up to $K_{0.5}VOPO_4$ after which $V_{trans}O_6$ oxidizes to V^{5+}. Since our previous work demonstrated that $KVPO_4F_{0.5}O_{0.5}$ can be described as a solid solution of the $KVPO_4F$—$KVOPO_4$

binary system, it is likely that its electrochemical mechanism can be explained through those of its parent compositions.[11,42] In order to calculate the density of electronic states, the experimental crystal structure of $KVPO_4F$ was used as the starting model. The $K_{0.5}VPO_4F$ and K_0VPO_4F structures were built using the experimental structure of $KVPO_4F$ with the following K distribution hypothesis:

- $K_{0.5}VPO_4F$ with only K(1) site occupied and K(2) fully depopulated;
- $K_{0.5}VPO_4F$ with only K(2) site occupied and K(1) fully depopulated;
- $K_{0.5}VPO_4F$ with a random K(1) and K(2) site occupation;
- K_0VPO_4F with fully depopulated K(1) and K(2) sites.

After structural relaxation, the three $K_{0.5}VPO_4F$ structures have similar unit cell volumes with less than 1% variation (**Table S1)**. The most stable structure was found with occupied K(2) sites, consistently with previous results.[10] The hypothesis with occupied K(1) sites is destabilized by 38 meV/f.u and at last, the least stable structure is found with both K(2) and K(1) sites occupied (88 meV/f.u.) due to the stronger coulombic repulsion of close K(1) and K(2) atoms. The total density of states (DOS) and partial density of states (pDOS) of the two symmetry inequivalent V sites are thus displayed in **Figure 6** for $K_{0.5}VPO_4F$ with occupied K(2) sites, and compared with those of $KVPO_4F$ and K_0VPO_4F. In $KVPO_4F$, the occupied electronic states close to the Fermi level, in the -1 to 0 eV range, have a predominant metal character corresponding to the $3d^2$ electrons of the valence band. Interestingly, $V(1)_{cis}$ occupied *d* states are located just below the Fermi level whereas the ones of $V(2)_{trans}$ are 0.5 eV lower in energy (**Figure 6a**). Nevertheless, the shape of isosurface spin density maps is characteristic of degenerated d_{xy}, d_{xz}, and d_{yz} orbitals forming the t_{2g} level. Considering a rigid band model upon charge, we expect the oxidation of the $V(1)_{cis}$ site before that of $V(2)_{trans}$. When the K(1) site is fully depopulated, which corresponds to the most stable structure for the composition $K_{0.5}VPO_4F$, the Fermi level is now located at the top of $V(2)_{trans}$ *d* pDOS (**Figure 6b)** and $V(1)_{cis}$ is oxidized to the +4 state. The spin density map of the latter site corresponds to a single d_{yz} type orbital (arbitrary choice) which depicts a lifting of the t_{2g} degeneracy. Note that this charge ordering is not related to the occupancy of K sites since similar calculations with only occupied K(1) sites or a statistical distribution among K(1) and K(2) sites all yielded similar results. Lastly, full removal of K^+ ions is accompanied by the oxidation of $V(2)_{trans}$ site to V^{4+} as witnessed by spin density maps. Again, the occupied *d* states of $V(1)_{cis}$ are located at a higher energy than those of $V(2)_{trans}$, which tends to confirm that the KTP structure exhibits a higher redox potential for the *trans* transition metal site than for the *cis* site.

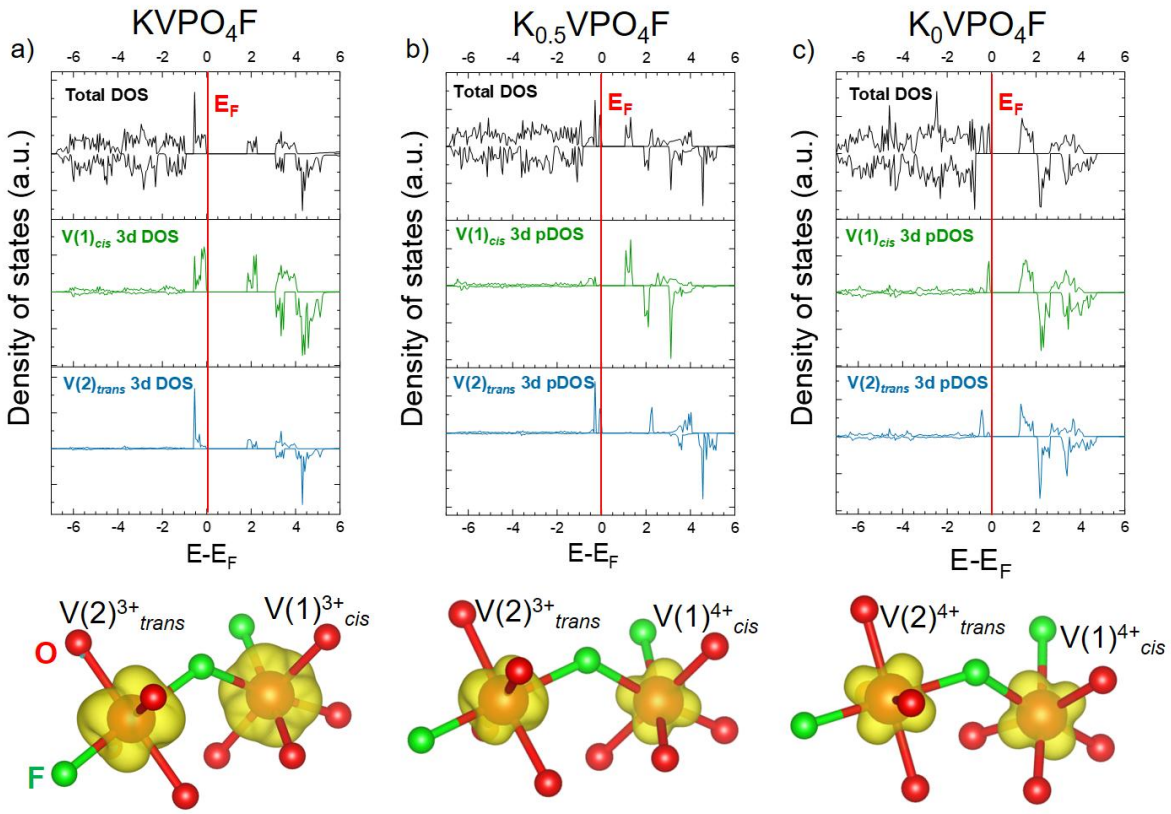

Figure 6: Total DOS and V site selected 3*d* pDOS of a) $KVPO_4F$, b) $K_{0.5}VPO_4F$ (K(2) site occupied) and c) K_0VPO_4F. The spin density maps of the corresponding V sites are shown below at isosurface value of 10^{-2} spins·Å^{-3}.

Preferential oxidation in KTP structured compounds

Previous experimental work on $KTiPO_4F$[43] and $KFeSO_4F$[44] as well as computational work on $KVOPO_4$,[42] all of these compounds adopting the KTP-type structure, have also shown that the charge compensation mechanism is sequential. For $KFeSO_4F$, it was demonstrated by *in situ* Mössbauer spectroscopy that one Fe site is oxidized before the other, with however an uncertain assignment. For the pristine composition $KTiPO_4F$, Fedotov and co-workers showed by DFT calculations that the Fermi level was located on top of the electron band having a *cis* TiO_4F_2 character, while the electrons with *trans* TiO_4F_2 character were located 0.25 eV lower in energy. These findings are similar to the results just discussed for K_xVPO_4F (x = 0, 0.5, 1). One could conclude that the *cis* arrangement of F^- ligands is destabilizing the *d* levels of V and Ti compared to the *trans* arrangement. However, it fails to describe the sequential oxidation in $KVOPO_4$ since all ligands are oxides. In an attempt to understand the origin of preferential oxidation in KTP compounds, we tried to disentangle the electrostatic contribution from the structure and the hybridization effect from the ligands on the position of the V 3*d* levels.

Firstly, empirical orbital diagrams for regular *cis* and *trans* $V^{3+}O_4F_2$ octahedra were established by considering the difference in electronegativity of F and O ligands (**Figure S13**). It results in a noticeable difference, with the t_{2g} orbital degeneracy slightly raised. For *trans* VO_4F_2, the stabilized $d_{xz,yz}$ orbitals are half filled, whereas the destabilized d_{xy} is empty. For *cis* VO_4F_2, the stabilized d_{xz} is filled and the destabilized $d_{xy,yz}$ contain one electron. Thus, in an hypothetical material containing both environments, removing an electron from the upper levels of the band structure (*i.e.* with antibonding V_{cis} $3d_{xy,yz}$ character) would result in the oxidation of *cis* site. These electronic considerations were further confirmed by calculating the V 3d *l*- and *m*-projected pDOS of hypothetical perovskite $SrV^{3+}O_2F$ structures with either *cis* or *trans* arrangement of fluorine anions (**Tables S2** and **S3**). This

chemical composition was chosen due to the possibility to arrange O/F anions in *trans* (single cell is sufficient) or *cis* (2×2×2 supercell is necessary) configuration around V^{3+} and also because the tolerance factor is 0.975, *i.e.*, it is a cubic perovskite. Thus, we can monitor the influence of O/F configuration on the electronic structure in a symmetric crystal structure without any tilt or distortion. The calculations were performed using GGA+U method with U_{eff} = 3 eV and the obtained pDOS (**Figure 7**) agrees with the empirical orbital diagrams proposed in **Figure S13**.

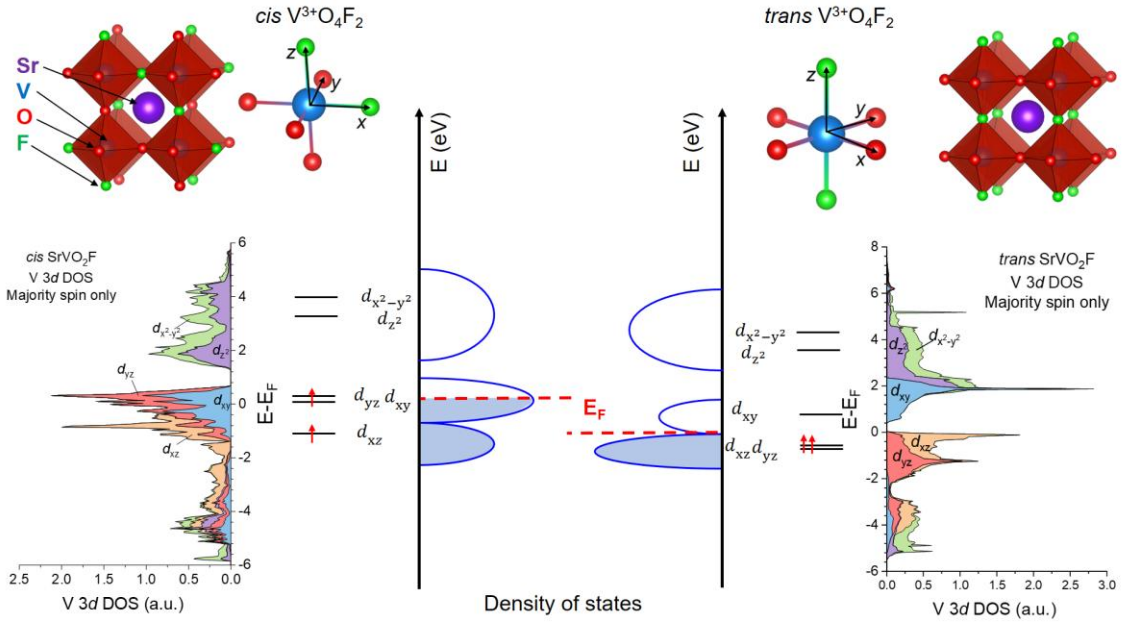

Figure 7: Hypothetical crystal structures of *cis* and *trans* $SrVO_2F$ together with their corresponding projected V 3*d* density of states and schematic band diagram.

Subsequently, the purely electrostatic contribution calculated from the Madelung site potential by considering formal oxidation states was evaluated with the MADEL program, implemented in the VESTA software.[26] The experimental XRD refined structure of $KVPO_4F$ was used and yielded electric potential of -33.67 V at the $V(1)_{cis}$ site and -32.81 V at the $V(2)_{trans}$ site. Thus, the V 3*d* levels of the two sites are not expected to lie at the same energy in $KVPO_4F$ with a difference of about 0.86 eV (**Figure 8**). To this purely electrostatic effect, one must also consider the superposition of metal-ligand covalency and hybridization, band structure dispersion and small distortions. Experimentally, the lower part of the voltage curve of K_xVPO_4F has an average voltage of 4.2 V vs K^+/K whereas the upper redox activity lies at 4.8 V vs K^+/K, corresponding to a stabilization of 0.6 eV for the *trans* site compared to *cis* in the rigid band approximation.

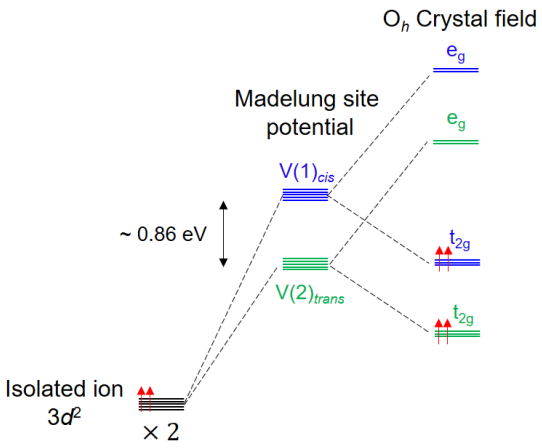

Figure 8: Schematic diagram of the V 3*d* energy levels in $KVPO_4F$.

Ex situ X-ray Diffraction

Ex situ XRD refinements were performed on a positive electrode recovered after charging a K//$KVPO_4F$ battery at 4.6 V vs K^+/K (**Figure S14**), in order to distinguish the *cis* and *trans* site reaction pathways after K^+ de-intercalation and compare the experimental data with previously discussed calculations. The resulting XRD pattern was refined with the Rietveld method (**Figure 9a**) in the *Pna*2_1 space group. The atomic positions and site occupancies are given in **Table S4**. The refinement of K sites positions and occupancies yields the composition $K_{0.47}VPO_4F$ where the "K1" site is fully depopulated and the K2 site is populated at 93 %. The K^+-vacancy ordering obtained from refinement is in very good agreement with the most stable calculated arrangement, corresponding to the K2 site fully occupied for the $K_{0.5}VPO_4F$ composition. Besides, the vanadium local environments resulting from XRD analysis slightly deviate from pure octahedral symmetry with a more distorted site for $V^{4+}{}_{cis}$ (**Table S4**). The calculation of their bond valence sum (BVS) yields 3.83 for the *cis* and 3.00 for the *trans* V sites. Finally, the bond lengths of the V^{4+}*cis* site average to 1.94 Å, which is in very good agreement with the 1.94 Å average ones refined from EXAFS fitting, while the average bond length of V_{trans} remains 2.02 Å. Overall, these findings confirm the preferential oxidation of the *cis* site compared to the *trans* VO_4F_2.

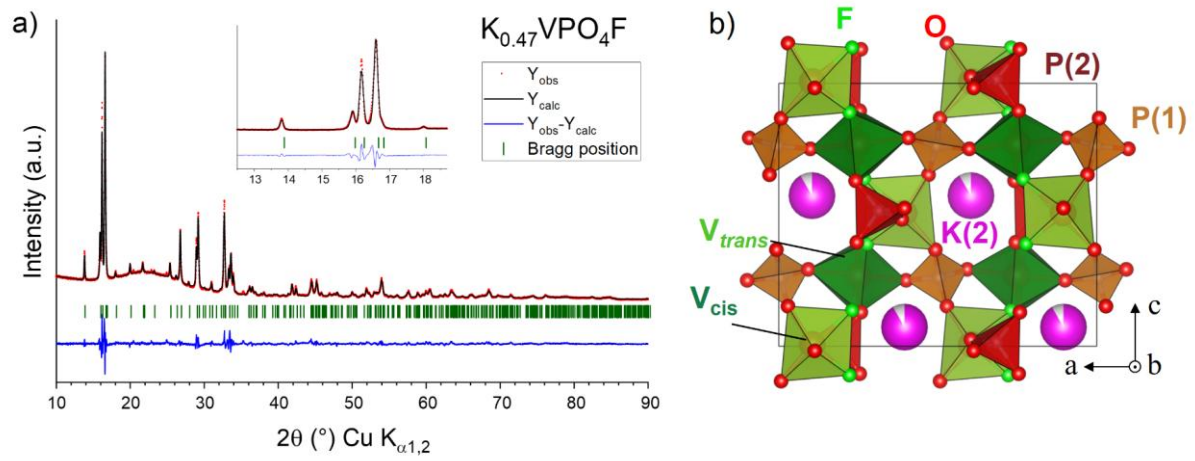

Figure 9: a) Rietveld refinement of the material recovered from K//$KVPO_4F$ battery charged to 4.6 V vs K^+/K. R_p=3.12%, R_{wp}=4.58%, χ^2=3.08%. b) Crystal structure described in *Pna*2_1 space group and visualisation of the position of K sites.

Discussion

The full redox mechanism of charge compensation during the de-intercalation of $K_xVPO_4F_{0.5}O_{0.5}$ is inherently very complex due to anion disorder. Indeed, one can count eight different V local environments depending on the site ($V1_{cis}$ or $V2_{trans}$), and the coordination ($V^{3+}O_4F_2$, $V^{3+}O_5F$, $\{V^{4+}{=}O\}O_5$ and $\{V^{4+}{=}O\}O_4F$). Even though it is not possible to disentangle such a complexity only on the basis of the experimental results, our findings combining these results with a theoretical approach can help proposing a possible redox mechanism. First, *operando* XAS shows that the charge transfer upon K^+ de-intercalation from $K_xVPO_4F_{0.5}O_{0.5}$ is first balanced by the oxidation of V^{3+} to V^{4+} in the composition range such as $0.5 < x < 1$ and then by oxidation of $V^{4+}{=}O$ to $V^{5+}{=}O$ for $x < 0.5$. Furthermore, this work as well as the one of Lian *et. al*[42] indicate that the V_{cis} site is systematically oxidized before V_{trans} in $KVPO_4F$ and $KVOPO_4$, respectively. Lastly, we can naturally consider V—F

bonds to possess a more ionic character than V—O ones such that for a given *cis* or *trans* site, and for V^{3+} and V^{4+}=O, the configuration with the larger number of oxygens should result in lower redox potential of the oxidized V site. By combining all these considerations, a schematic redox mechanism is reported in **Figure 10**, which shows the proposed sequence for the oxidation of the different V environments. Our model does not take into account the interaction that a given V site has with its two V neighbours, which would result in 32 different configurations. Consequently, the proposed redox mechanism should not be perceived as a rigid sequential mechanism but rather as an oxidation sequence likelihood diagram. This model is in very good agreement with the solid solution-like electrochemical curve of $KVPO_4F_{0.5}O_{0.5}$ which was previously attributed to structural disorder and can now be further argued to also originate from a continuum of V states energies in the electronic structure.

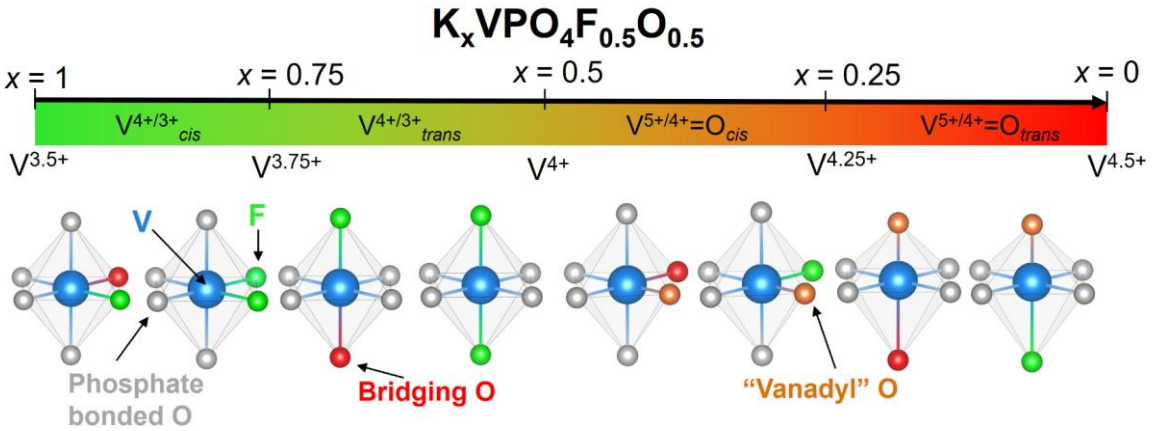

Figure 10: Proposition of a possible full redox mechanism of $K_xVPO_4F_{0.5}O_{0.5}$. The different vanadium local environments are arranged according to their lower expected redox potential (left) to the highest (right).

CONCLUSION

In this study we applied *operando* V K-edge XAS to probe the redox mechanism of $KVPO_4F$, $KVOPO_4$ and $KVPO_4F_{0.5}O_{0.5}$ used as KIB positive electrode materials. In $KVPO_4F$ and $KVOPO_4$, the de-insertion of K^+ ions is compensated by the activation of $V^{4+/3+}$ and $\{V^{5+/4+}=O\}$ redox couples, respectively. The qualitative analysis of the XANES spectra and the refinements of the EXAFS oscillations of $KVPO_4F_{0.5}O_{0.5}$ highlight the successive activation of $V^{4+/3+}$ below 4.6 V vs K^+/K followed by $\{V^{5+/4+}=O\}$ in the high potential region up to 5 V. Furthermore, we experimentally demonstrate by XRD the sequential oxidation of *cis* V site before *trans* V site upon charge in $KVPO_4F$ as predicted by *ab initio* calculations. This site sequential activation originates from the specificity of the KTP-type crystal structure which induces a Madelung potential difference close to 1 V between the $V(1)_{cis}$ and $V(2)_{trans}$ sites as well as the effect of F ligands configuration on the electronic structure. The latter was demonstrated on the basis of *ab initio* calculations of the electronic structures of *cis* and *trans* $SrVO_2F$ perovskites. Finally, by combining all the above-mentioned findings, we propose a description of the macroscopic electrochemical signature by a microscopically resolved redox mechanism of $K_xVPO_4F_{0.5}O_{0.5}$ where eight different V environments oxidize sequentially, thus explaining the observed solid solution-like electrochemical curve. It would be interesting to compare the prediction of this site-sequential oxidation in $K_xVPO_4F_{1-y}O_y$ with *ab initio* calculations, where the effect of K^+ and O/F distribution on the electronic structure could be more deeply understood.

AUTHOR INFORMATION

Corresponding authors

Laurence Croguennec – Univ. Bordeaux, CNRS, Bordeaux INP, ICMCB, UMR 5026, F-33600 Pessac, France; RS2E, Réseau sur le Stockage Electrochimique de l'Energie, FR CNRS 3459, Amiens F-80039 Cedex 1, France; ALISTORE-ERI European Research Institute, FR CNRS 3104, F-80039 Amiens Cedex 1, France; orcid.org/0000-0002-3018-0992; Email: Laurence.Croguennec@icmcb.cnrs.fr

Dany Carlier – Univ. Bordeaux, CNRS, Bordeaux INP, ICMCB, UMR 5026, F-33600 Pessac, France; RS2E, Réseau sur le Stockage Electrochimique de l'Energie, FR CNRS 3459, Amiens F-80039 Cedex 1, France; ALISTORE-ERI European Research Institute, FR CNRS 3104, F-80039 Amiens Cedex 1, France; orcid.org/0000-0002-5086-4363; Email: Dany.Carlier@icmcb.cnrs.fr

Authors

Romain Wernert – Univ. Bordeaux, CNRS, Bordeaux INP, ICMCB, UMR 5026, F-33600 Pessac, France; ICGM, Univ. Montpellier, CNRS, ENSCM, Montpellier, France; RS2E, Réseau sur le Stockage Electrochimique de l'Energie, FR CNRS 3459, Amiens F-80039 Cedex 1, France; orcid.org/0000-0002-5073-4008

Antonella Iadecola – RS2E, Réseau sur le Stockage Electrochimique de l'Energie, FR CNRS 3459, Amiens F-80039 Cedex 1, France; orcid.org/0000-0002-9031-8455

Lorenzo Stievano – ICGM, Univ. Montpellier, CNRS, ENSCM, Montpellier, France; RS2E, Réseau sur le Stockage Electrochimique de l'Energie, FR CNRS 3459, Amiens F-80039 Cedex 1, France; ALISTORE-ERI European Research Institute, FR CNRS 3104, F-80039 Amiens Cedex 1, France; orcid.org/0000-0001-8548-0231

SUPPORTING INFORMATION

Electrochemical cycling curves of the operando experiments, additional XANES spectra comparison, EXAFS fits of $KVOPO_4$ and $KVPO_4F$, molecular orbital diagrams, DFT relaxed structures of *cis* and *trans* $SrVO_2F$, electrochemical curve of the sample recovered for ex-situ XRD, full pattern matching and atomic parameters of $K_{0.52}VPO_4F$.

ACKNOWLEDGEMENTS

This work was part of the TROPIC project supported by Agence Nationale de la Recherche (ANR) under the grant ANR-19-CE05-0026. ANR is also acknowledged for funding the RS2E network through the STORE-EX Labex Project ANR-10-LABX-76-01. Synchrotron Soleil (France) is acknowledged for providing beamtime (proposal #20191774) at the beamline ROCK which also benefits from ANR grant as part of the "Investissements d'Avenir" program ANR-10-EQPX-45. The authors are thankful to Laure Monconduit (ICGM) and Alain Demourgues (ICMCB) for fruitful discussions.

REFERENCES

(1) Hosaka, T.; Kubota, K.; Hameed, A. S.; Komaba, S. Research Development on K-Ion Batteries. *Chem. Rev.* **2020**, *120* (14), 6358–6466. https://doi.org/10.1021/acs.chemrev.9b00463.

(2) Shao, L.; Jin, S. Resilience Assessment of the Lithium Supply Chain in China under Impact of New Energy Vehicles and Supply Interruption. *Journal of Cleaner Production* **2020**, *252*, 119624. https://doi.org/10.1016/j.jclepro.2019.119624.

(3) Rudnick, R. L.; Gao, S. Composition of the Continental Crust. In *Treatise on Geochemistry*; Elsevier, 2003; pp 1–64. https://doi.org/10.1016/B0-08-043751-6/03016-4.

(4) Komaba, S.; Hasegawa, T.; Dahbi, M.; Kubota, K. Potassium Intercalation into Graphite to Realize High-Voltage/High-Power Potassium-Ion Batteries and Potassium-Ion Capacitors. *Electrochemistry Communications* **2015**, *60*, 172–175. https://doi.org/10.1016/j.elecom.2015.09.002.

(5) Marcus, Y. ANALYTICAL CHEMISTRY DIVISION COMMISSION ON ELECTROANALYTICAL CHEMISTRY. In *Classification and Nomenclature of Electroanalytical Techniques*; Elsevier, 1976; pp 83–95. https://doi.org/10.1016/B978-0-08-021226-5.50002-2.

(6) Hosaka, T.; Shimamura, T.; Kubota, K.; Komaba, S. Polyanionic Compounds for Potassium- Ion Batteries. *Chem. Rec.* **2019**, *19* (4), 735–745. https://doi.org/10.1002/tcr.201800143.

(7) Chihara, K.; Katogi, A.; Kubota, K.; Komaba, S. $KVPO_4F$ and $KVOPO_4$ toward 4 Volt-Class Potassium-Ion Batteries. *Chem. Commun.* **2017**, *53* (37), 5208–5211. https://doi.org/10.1039/C6CC10280H.

(8) Fedotov, S. S.; Khasanova, N. R.; Samarin, A. Sh.; Drozhzhin, O. A.; Batuk, D.; Karakulina, O. M.; Hadermann, J.; Abakumov, A. M.; Antipov, E. V.

$AVPO_4F$ (A = Li, K): A 4 V Cathode Material for High-Power Rechargeable Batteries. *Chem. Mater.* **2016**, *28* (2), 411–415. https://doi.org/10.1021/acs.chemmater.5b04065.

(9) Chihara, K.; Katogi, A.; Kubota, K.; Komaba, S. $KVPO_4F$ and $KVOPO_4$ toward 4 Volt-Class Potassium-Ion Batteries. *Chem. Commun.* **2017**, *53* (37), 5208–5211. https://doi.org/10.1039/C6CC10280H.

(10) Kim, H.; Seo, D.-H.; Bianchini, M.; Clément, R. J.; Kim, H.; Kim, J. C.; Tian, Y.; Shi, T.; Yoon, W.-S.; Ceder, G. A New Strategy for High-Voltage Cathodes for K-Ion Batteries: Stoichiometric $KVPO_4F$. *Adv. Energy Mater.* **2018**, *8* (26), 1801591. https://doi.org/10.1002/aenm.201801591.

(11) Wernert, R.; Nguyen, L. H. B.; Petit, E.; Camacho, P. S.; Iadecola, A.; Longo, A.; Fauth, F.; Stievano, L.; Monconduit, L.; Carlier, D.; Croguennec, L. Controlling the Cathodic Potential of $KVPO_4F$ through Oxygen Substitution. *Chem. Mater.* **2022**, *34* (10), 4523–4535. https://doi.org/10.1021/acs.chemmater.2c00295.

(12) Saubanère, M.; Yahia, M. B.; Lebègue, S.; Doublet, M.-L. An Intuitive and Efficient Method for Cell Voltage Prediction of Lithium and Sodium-Ion Batteries. *Nat Commun* **2014**, *5* (1), 5559. https://doi.org/10.1038/ncomms6559.

(13) Boivin, E.; Iadecola, A.; Fauth, F.; Chotard, J.-N.; Masquelier, C.; Croguennec, L. Redox Paradox of Vanadium in Tavorite $LiVPO_4F_{1-y}O_y$. *Chem. Mater.* **2019**, *31* (18), 7367–7376. https://doi.org/10.1021/acs.chemmater.9b01987.

(14) Nguyen, L. H. B.; Iadecola, A.; Belin, S.; Olchowka, J.; Masquelier, C.; Carlier, D.; Croguennec, L. A Combined Operando Synchrotron X-Ray Absorption Spectroscopy and First-Principles Density Functional Theory Study to Unravel the Vanadium Redox Paradox in the $Na_3V_2(PO_4)_2F_3$–$Na_3V_2(PO_4)_2FO_2$ Compositions. *J. Phys. Chem. C* **2020**, *124* (43), 23511–23522. https://doi.org/10.1021/acs.jpcc.0c06967.

(15) Broux, T.; Bamine, T.; Simonelli, L.; Stievano, L.; Fauth, F.; Ménétrier, M.; Carlier, D.; Masquelier, C.; Croguennec, L. V^{IV} Disproportionation Upon Sodium Extraction From $Na_3V_2(PO_4)_2F_3$ Observed by Operando X-Ray Absorption Spectroscopy and Solid-State NMR. *J. Phys. Chem. C* **2017**, *121* (8), 4103–4111. https://doi.org/10.1021/acs.jpcc.6b11413.

(16) Park, S.; Chotard, J.-N.; Carlier, D.; Moog, I.; Duttine, M.; Fauth, F.; Iadecola, A.; Croguennec, L.; Masquelier, C. An Asymmetric Sodium Extraction/Insertion Mechanism for the Fe/V-Mixed NASICON $Na_4FeV(PO_4)_3$. *Chem. Mater.* **2022**, acs.chemmater.2c00501. https://doi.org/10.1021/acs.chemmater.2c00501.

(17) Leriche, J. B.; Hamelet, S.; Shu, J.; Morcrette, M.; Masquelier, C.; Ouvrard, G.; Zerrouki, M.; Soudan, P.; Belin, S.; Elkaïm, E.; Baudelet, F. An Electrochemical Cell for Operando Study of Lithium Batteries Using Synchrotron Radiation. *J. Electrochem. Soc.* **2010**, *157* (5), A606. https://doi.org/10.1149/1.3355977.

(18) Lesage, C.; Devers, E.; Legens, C.; Fernandes, G.; Roudenko, O.; Briois, V. High Pressure Cell for Edge Jumping X-Ray Absorption Spectroscopy: Applications to Industrial Liquid Sulfidation of Hydrotreatment Catalysts. *Catalysis Today* **2019**, *336*, 63–73. https://doi.org/10.1016/j.cattod.2019.01.081.

(19) Jaumot, J.; de Juan, A.; Tauler, R. MCR-ALS GUI 2.0: New Features and Applications. *Chemometrics and Intelligent Laboratory Systems* **2015**, *140*, 1–12. https://doi.org/10.1016/j.chemolab.2014.10.003.

(20) de Juan, A.; Jaumot, J.; Tauler, R. Multivariate Curve Resolution (MCR). Solving the Mixture Analysis Problem. *Anal. Methods* **2014**, *6* (14), 4964–4976. https://doi.org/10.1039/C4AY00571F.

(21) Fehse, M.; Iadecola, A.; Sougrati, M. T.; Conti, P.; Giorgetti, M.; Stievano, L. Applying Chemometrics to Study Battery Materials: Towards the Comprehensive Analysis of Complex Operando Datasets. *Energy Storage Materials* **2019**, *18*, 328–337. https://doi.org/10.1016/j.ensm.2019.02.002.

(22) Petříček, V.; Dušek, M.; Palatinus, L. Crystallographic Computing System JANA2006: General Features. *Zeitschrift für Kristallographie - Crystalline Materials* **2014**, *229* (5), 345–352. https://doi.org/10.1515/zkri-2014-1737.

(23) Baur, W. H. The Geometry of Polyhedral Distortions. Predictive Relationships for the Phosphate Group. *Acta Crystallogr B Struct Sci* **1974**, *30* (5), 1195–1215. https://doi.org/10.1107/S0567740874004560.

(24) Bérar, J.-F.; Lelann, P. E.s.d.'s and Estimated Probable Error Obtained in Rietveld Refinements with Local Correlations. *Journal of Applied Crystallography* **1991**, *24* (1), 1–5. https://doi.org/10.1107/S0021889890008391.

(25) Rodríguez-Carvajal, J. Recent Advances in Magnetic Structure Determination by Neutron Powder Diffraction. *Physica B: Condensed Matter* **1993**, *192* (1–2), 55–69. https://doi.org/10.1016/0921-4526(93)90108-I.

(26) Momma, K.; Izumi, F. *VESTA* : A Three-Dimensional Visualization System for Electronic and Structural Analysis. *J Appl Crystallogr* **2008**, *41* (3), 653–658. https://doi.org/10.1107/S0021889808012016.

(27) Kresse, G.; Joubert, D. From Ultrasoft Pseudopotentials to the Projector Augmented-Wave Method. *Physical Review B* **1999**, *59* (3), 1758–1775. https://doi.org/10.1103/PhysRevB.59.1758.

(28) Blöchl, P. E. Projector Augmented-Wave Method. *Physical Review B* **1994**, *50* (24), 17953–17979. https://doi.org/10.1103/PhysRevB.50.17953.

(29) Kresse, G.; Hafner, J. Ab Initio Molecular Dynamics for Liquid Metals. *Physical Review B* **1993**, *47* (1), 558–561. https://doi.org/10.1103/PhysRevB.47.558.

(30) Kresse, G.; Furthmüller, J. Efficiency of Ab-Initio Total Energy Calculations for Metals and Semiconductors Using a Plane-Wave Basis Set. *Computational Materials Science* **1996**, *6* (1), 15–50. https://doi.org/10.1016/0927-0256(96)00008-0.

(31) Kresse, G.; Hafner, J. Ab Initio Molecular-Dynamics Simulation of the Liquid-Metalamorphous- Semiconductor Transition in

Germanium. *Physical Review B* **1994**, *49* (20), 14251–14269. https://doi.org/10.1103/PhysRevB.49.14251.
(32) Kresse, G.; Furthmüller, J. Efficient Iterative Schemes for Ab Initio Total-Energy Calculations Using a Plane-Wave Basis Set. *Physical Review B - Condensed Matter and Materials Physics* **1996**, *54* (16), 11169–11186. https://doi.org/10.1103/PhysRevB.54.11169.
(33) Perdew, J. P.; Burke, K.; Ernzerhof, M. Generalized Gradient Approximation Made Simple. *Physical Review Letters* **1996**, *77* (18), 3865–3868. https://doi.org/10.1103/PhysRevLett.77.3865.
(34) Dudarev, S.; Botton, G. Electron-Energy-Loss Spectra and the Structural Stability of Nickel Oxide: An LSDA+U Study. *Physical Review B - Condensed Matter and Materials Physics*. 1998, pp 1505–1509. https://doi.org/10.1103/PhysRevB.57.1505.
(35) Wang, L.; Maxisch, T.; Ceder, G. Oxidation Energies of Transition Metal Oxides within the GGA + U Framework. *Phys. Rev. B* **2006**, *73* (19), 195107. https://doi.org/10.1103/PhysRevB.73.195107.
(36) Caracciolo, L.; Madec, L.; Petit, E.; Gabaudan, V.; Carlier, D.; Croguennec, L.; Martinez, H. Electrochemical Redox Processes Involved in Carbon-Coated $KVPO_4F$ for High Voltage K-Ion Batteries Revealed by XPS Analysis. *J. Electrochem. Soc.* **2020**, *167* (13), 130527. https://doi.org/10.1149/1945-7111/abbb0c.
(37) Kim, H.; Tian, Y.; Ceder, G. Origin of Capacity Degradation of High-Voltage $KVPO_4F$ Cathode. *J. Electrochem. Soc.* **2020**, *167* (11), 110555. https://doi.org/10.1149/1945-7111/aba54e.
(38) Wernert, R.; Nguyen, L. H. B.; Iadecola, A.; Weill, F.; Fauth, F.; Monconduit, L.; Carlier, D.; Croguennec, L. Self-Discharge Mechanism of High-Voltage KVPO4F for K-Ion Batteries. *ACS Appl. Energy Mater.* **2022**. https://doi.org/10.1021/acsaem.2c02379.
(39) Boivin, E.; David, R.; Chotard, J.-N.; Bamine, T.; Iadecola, A.; Bourgeois, L.; Suard, E.; Fauth, F.; Carlier, D.; Masquelier, C.; Croguennec, L. $LiVPO_4F_{1-y}O_y$ Tavorite-Type Compositions: Influence of the Concentration of Vanadyl-Type Defects on the Structure and Electrochemical Performance. *Chem. Mater.* **2018**, *30* (16), 5682–5693. https://doi.org/10.1021/acs.chemmater.8b02138.
(40) Broux, T.; Bamine, T.; Fauth, F.; Simonelli, L.; Olszewski, W.; Marini, C.; Ménétrier, M.; Carlier, D.; Masquelier, C.; Croguennec, L. Strong Impact of the Oxygen Content in $Na_3V_2(PO_4)_2F_{3-y}O_y$ ($0 \leq y \leq 0.5$) on Its Structural and Electrochemical Properties. *Chem. Mater.* **2016**, *28* (21), 7683–7692. https://doi.org/10.1021/acs.chemmater.6b02659.
(41) Ouvrard, G.; Zerrouki, M.; Soudan, P.; Lestriez, B.; Masquelier, C.; Morcrette, M.; Hamelet, S.; Belin, S.; Flank, A. M.; Baudelet, F. Heterogeneous Behaviour of the Lithium Battery Composite Electrode $LiFePO_4$. *Journal of Power Sources* **2013**, *229*, 16–21. https://doi.org/10.1016/j.jpowsour.2012.11.057.
(42) Lian, R.; Wang, D.; Ming, X.; Zhang, R.; Wei, Y.; Feng, J.; Meng, X.; Chen, G. Phase Transformation, Ionic Diffusion, and Charge Transfer Mechanisms of $KVOPO_4$ in Potassium Ion Batteries: First-Principles Calculations. *J. Mater. Chem. A* **2018**, *6* (33), 16228–16234. https://doi.org/10.1039/C8TA06708B.
(43) Fedotov, S. S.; Luchinin, N. D.; Aksyonov, D. A.; Morozov, A. V.; Ryazantsev, S. V.; Gaboardi, M.; Plaisier, J. R.; Stevenson, K. J.; Abakumov, A. M.; Antipov, E. V. Titanium-Based Potassium-Ion Battery Positive Electrode with Extraordinarily High Redox Potential. *Nat Commun* **2020**, *11* (1), 1484. https://doi.org/10.1038/s41467-020-15244-6.
(44) Recham, N.; Rousse, G.; Sougrati, M. T.; Chotard, J.-N.; Frayret, C.; Mariyappan, S.; Melot, B. C.; Jumas, J.-C.; Tarascon, J.-M. Preparation and Characterization of a Stable $FeSO_4F$-Based Framework for Alkali Ion Insertion Electrodes. *Chem. Mater.* **2012**, *24* (22), 4363–4370. https://doi.org/10.1021/cm302428w.

TOC graphic

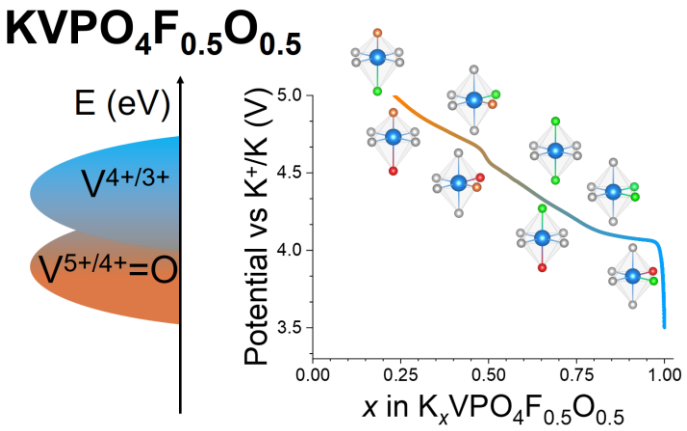
KVPO4F0.5O0.5
E (eV)
V4+/3+
V5+/4+=O
Potential vs K+/K (V)
5.0
4.5
4.0
3.5
0.00
0.25
0.50
0.75
1.00
x in KxVPO4F0.5O0.5